12

Ultrafast Photoelectric Effect in Oxide Single Crystals and Films

Hao Ni and Kun Zhao
Laboratory of Optic Sensing and Detecting Technology,
China University of Petroleum, Beijing
People's Republic of China

1. Introduction

In recent years there has been an increasing demand for detecting the ultrafast laser pulse to apply in environmental monitoring such as solar ultraviolet (UV) radiation monitoring, ozone-hole sensing, flame detection for a fire alarm, and secure space-to-space communication and many research groups focus their attention on the detector materials and its various kinds of detecting performance parameter. Main efforts are currently directed to wide band gap semiconductors, such as III-V nitrides,[1] silicon carbide,[2] zinc oxide,[3] and diamond,[4] which are a much more attractive choice for selective UV detection. A response of 8 ns rise time and 1.4 μs fall time has been achieved in UV photoconductive detector based on epitaxial $Mg_{0.34}Zn_{0.66}O$ thin films.[5] Highly quality GaN devices exhibit 1.4-ps-wide electrical transients under illumination by 100 fs duration and 360 nm wavelength laser pulses.[6] In general, thermal detectors such as bolometers are independent of the wavelength with a major disadvantage of the slow response time, which limits their applications especially where the fast measurement is required. In the past few years, there have been active studies of the fast photoresponse of superconductor materials such as $YBa_2Cu_3O_{7-\delta}$ thin films irradiated by visible and infrared laser pulses, and the transport measurements of photo-induced voltages have probed the time scale from picosecond to nanosecond.[7-10] However, these devices require a complicated fabrication process and high-cost manufacturing.

In this paper, a brief review of our recent research results on oxide single crystals and films, such as tilted perovskite oxides,[11-13] polar crystals[14] and manganite films,[15,16] is presented. Some experimental results are introduced and then, theoretical investigations about interesting experimental phenomena are presented.

2. Ultrafast photovoltaic effects in oxide single crystals

2.1 Ultrafast photovoltaic effects in tilted perovskite oxide single crystals

Perovskite oxides, as one of the leading research topics, have been intensively studied due to their intrinsic properties such as insulating, ferroelectric, superconducting, colossal magnetoresistance, optical properties and so on. Some research groups focused their interests on the photoelectric effect of perovskite oxide materials, and the research results

showed that perovskite oxides have the potential and foreground as the photodetector materials in different wavelengths.

Strontium titanate oxide $SrTiO_3$ (STO) is a promising wide band gap material and appears to be excellent in the field of electronic industry. Over the years, STO has been mainly used for dielectric devices,[17–19] whereas very little work has been devoted to optical applications.[20,21] In agreement with its band gap of 3.2 eV, STO absorbs lights with a wave-length of less than 390 nm, presenting a high transparency in the visible and infrared wavelength range and selectively sensitive to a UV light.

As-supplied STO (001) single crystals with the purity of 99.99% are mirror double polished. The geometry of the sample is 3 mm × 10 mm with the thickness of 0.5 mm. The (001) plane is tilted as an angle of α with respect to the surface. The angles ranged from 0 to 45°. As shown in Fig. 1, the tilting of the c axis was confirmed by x-ray diffraction (XRD) measurement with the usual θ-2θ scan. To satisfy the Bragg's diffraction geometry, the [001] axis was aligned carefully and the offset point was set as ω. Here, ω was α or α-45° to detect (00*l*) or (*l*0*l*) peaks, respectively.

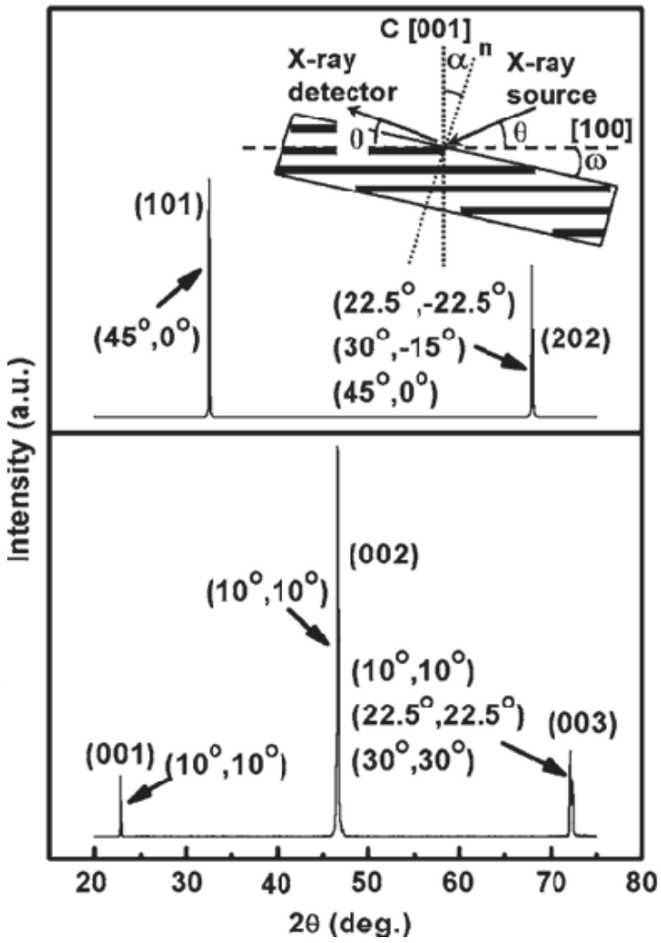

Fig. 1. X-ray diffraction patterns of tilted STO crystals. The inset shows the configuration of θ-2θ scan. To get different diffraction peaks, (00*l*), (101) and (202), ω was adjusted as shown in the angle arrays (α,ω) for different α. [11]

For the photovoltaic measurements, two indium electrodes separated by 1 mm were prepared on the laser-irradiated surface of the STO, and were always kept in the dark to prevent the generation of any electrical contact photovoltage. The third harmonic of an actively passively mode-locked Nd:yttrium–aluminum–garnet (Nd:YAG) laser was used as the light source, operating at a wavelength of 355 nm (3.49 eV photon energy) with 25 ps duration at a 1 Hz repetition rate and an energy density of 0.05 mJ mm^{-2} . Thus the on-sample energy is 0.15 mJ. The photovoltaic signals were monitored with a Tektronix sampling oscilloscope (2.5 GHz bandwidth) terminated into 1 MΩ.

The pulsed photovoltage was observed when the tilted STO surface was irradiated directly by a laser pulse. Figure 2(a) presents a typical transient open-circuit photovoltage of a 15° tilting STO single crystal. The peak photovoltage V_L^P is 52 mV, the 10%~90% rise time (RT) is 80 ns, and the full width at half maximum (FWHM) is 2.8 μs. To reduce the influence of the circuit in the measurement and the long tail of the decay time due to the RC effect in the photovoltaic signal, a 0.5 Ω load resistance was connected in the two electrodes and parallel with the STO crystal. As shown in Fig. 2(b), the RT is dramatically reduced to about 130 ps, which is limited by the oscilloscope, and the FWHM is also reduced to be about 230 ps. The peak photocurrent I_L^P is 4.7 mA, here, $I_L = V_L/0.5\ \Omega$.

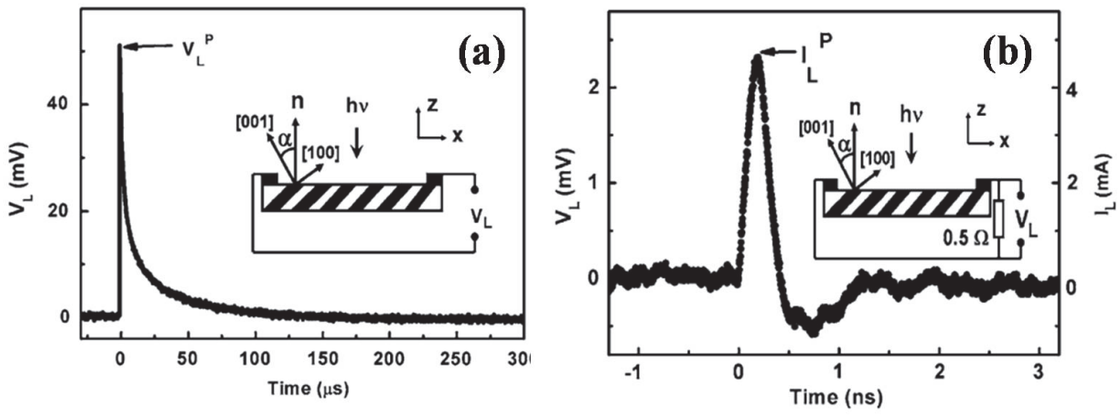

Fig. 2. (a) A typical open-circuit photovoltage and (b) a typical photoresponse signal with a 0.5 Ω resistance in parallel with the STO single crystal under an excitation of 25 ps duration and 355 nm laser pulses. The tilted degree α is 15°. The inset displays the schematic circuit of the measurement. V_L^P and I_L^P denote the peak value of the transient photovoltage and transient photocurrent, respectively. [11]

We did not observe the photovoltaic signal when the STO crystal was irradiated by the 532 or 632.8 nm pulse lasers. To characterize the photo-generated carriers of the samples used in present study, we determined the optical absorption spectrum from the optical transmission measurement using a SpectraPro500i spectrophometer. Figure 3 shows the UV-visible absorption spectrum of STO samples as a function of the wavelength. The sharp absorption edge is at ~385 nm, which is in agreement with the optical band gap of STO and the experimental results, indicating that photovoltaic signals cannot have been observed when the samples are irradiated by lasers with the photon energies smaller than the band gap of STO. This property demonstrates that the production of the photongenerated carriers plays a crucial role in the process of laser-induced voltage in this system.

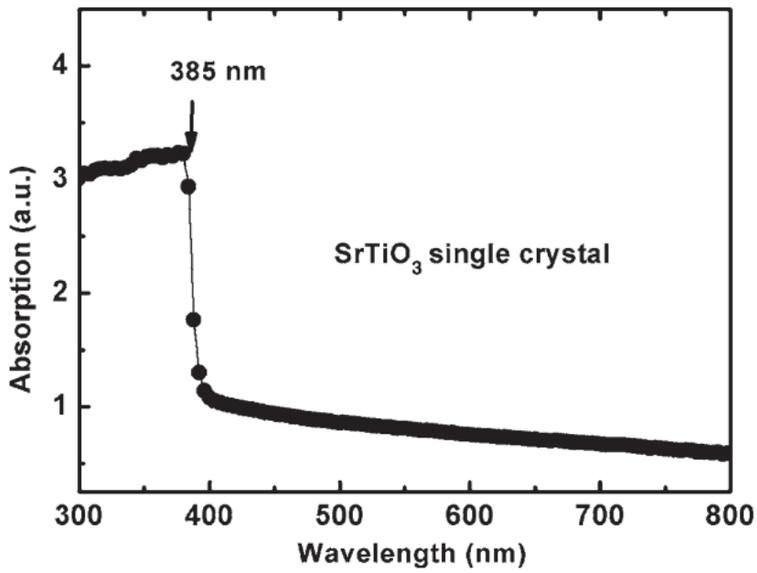

Fig. 3. Spectral absorption of STO single crystal with a thickness of 0.5 mm. [11]

To understand the mechanism of the photoelectric effect, we illuminate the STO crystal through the reverse face which is opposite to the side where leads are attached. The signal polarity reversal is obvious, and the response is essentially mirror images of each other. In addition, no photovoltage was generated along the nontilting [010] direction. These facts can be considered to support the suggestion that this phenomenon is due to a transverse thermoelectric effect.[22] In this case, the voltage can be represented by

$$E_x = l(S_{[100]} - S_{[001]})\sin(2\alpha)(dT/dz)/2. \quad (1)$$

Here l is the illumination length, $S_{[100]}$ and $S_{[001]}$ are the Seebeck coefficients along the [100] and [001] axis, and dT/dz is the temperature gradient in the direction of irradiation (the surface normal direction of STO crystal).

Furthermore, we chose several STO samples with different tilting angles (1°, 7°, 10°, 15°, 20°, 30°, 40°, 45°) and measured $V_L{}^P$ and $I_L{}^P$ as the function of α. The experimental procedures are the same as shown in Figs. 2(a) and 2(b). Results are plotted in Fig. 4. The signal amplitude increases with α until 20°, and then decreases. At α = 45°, the detected signal, similar to that at α = 0°, is basically a random noise due to the electrical-magnetical emission by the operation of the excimer laser. The maximum of the signal height, a photovoltage of 63 mV and a photocurrent of 67 mA, appears at α = 20°. It has been well known that each element of Seebeck tensor is proportional to the corresponding electrical resistivity of the system, and the electrical resistivity along each axis is reverse proportional to the transient carrier density correspondingly. In this way, Seebeck tensor strongly depends on the transient carrier density along each axis. The inset of Fig. 4 shows the schematic drawing under the irradiation of a UV pulse laser. If we divided the laser into two components of being parallel and being perpendicular to the tilting direction, the transient carrier density along each axis is proportional to the illuminated power perpendicular to the tilting direction, leading to $(S_{[100]} - S_{[001]}) \propto (\cos\alpha - \sin\alpha)$. So, we can get

$$E_x \propto l(\cos\alpha - \sin\alpha)\sin(2\alpha)(dT/dz)/2, \quad (2)$$

where the maximum occurs at α = 20.9°. From Fig. 3, we can see that the calculated results (dashed lines in Fig. 4) from Eq. 2 are in very good agreement with the measured points, which indicates that the present model of the mechanism for laser-induced voltage becomes convincing. This result also suggests the importance of the anisotropic thermoelectricity.

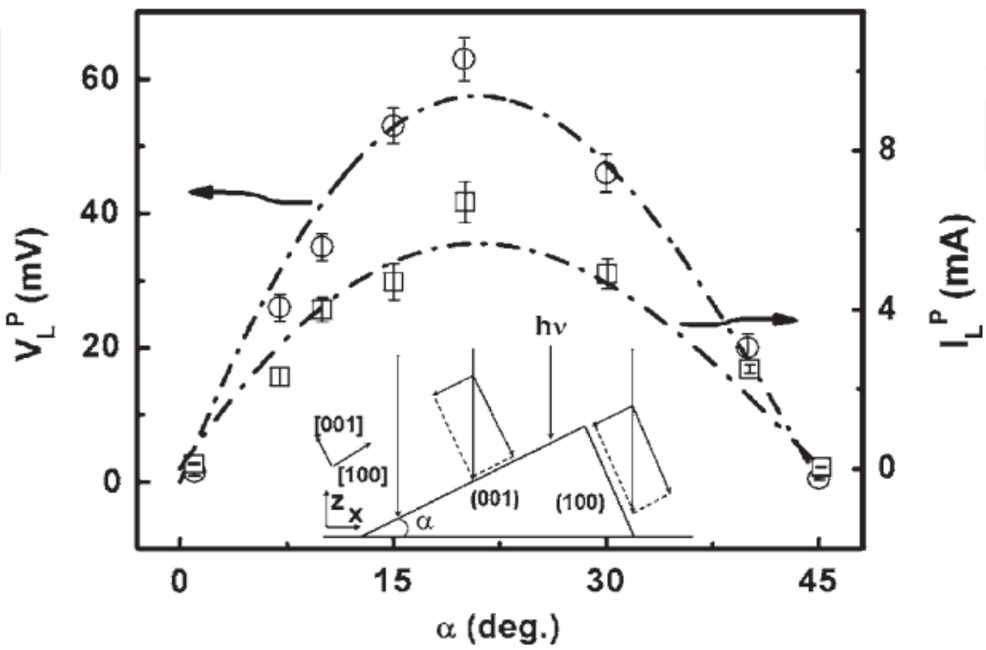

Fig. 4. Peak photovoltage (open circle) and peak photocurrent (open square) dependence of the tilting angle. The dashed lines show the fitting results using Eq. (2). [11]

To demonstrate the mechanism presented above, we also measured the irradiated area depended photovoltage, and the result showed that the measured voltage depended weakly on the length and linearly on the width of the irradiated area.[12] Figure 5(a) shows a diagram of the photoresponse measurement setup. The output of a Lambda Physik LEXTRA 200 XeCl excimer laser (308 nm wavelength, 20 ns pulse duration) was used as the laser source, with a single pulse energy density of 1.6 mJ/mm². The irradiated area was *wl*. The two electrodes were always kept in the dark to prevent any photovoltaic effect from the junctions. The photoresponse signal was monitored with a digital oscilloscope with 500 MHz resolution terminated into 50 Ω at ambient temperature.
Figure 6 displays the dependence of V_P on the irradiation area. For w = 3 mm and 10 mm, V_P is constant at ~ 0.05 V and ~ 0.15 V, respectively, independent of the value of l. However, V_P varies linearly with w for fixed l. Thus, from basic circuit theory, the total resistance in the l direction, can be expressed as

$$R_s = \frac{\rho l}{S} = \frac{\rho l}{wt} \tag{3}$$

Where ρ is the electrical resistivity along l direction and t is the thickness of the sample. Due to the configuration of the measurement setup (Fig. 5(b)), the circuit acts as a voltage divider, and the readout voltage V_T will be determined by

$$V_T = \frac{V_S R_T}{R_T + R_S} \approx \frac{V_S R_T}{R_S}, \tag{4}$$

where R_T = 50 Ω is the impedance at the input channel of the oscilloscope, and V_S is the actual signal generated by the sample, given by equations (2). Finally, according to the equation (2), one can obtain:

$$V_T \approx \frac{V_S R_T}{R_S} \propto \frac{R_T}{\frac{\rho l}{wt}} l(\cos\alpha - \sin\alpha)\sin(2\alpha)\frac{dT}{dz}\frac{1}{2} \propto w(\cos\alpha - \sin\alpha)\sin(2\alpha)\frac{dT}{dz}. \tag{5}$$

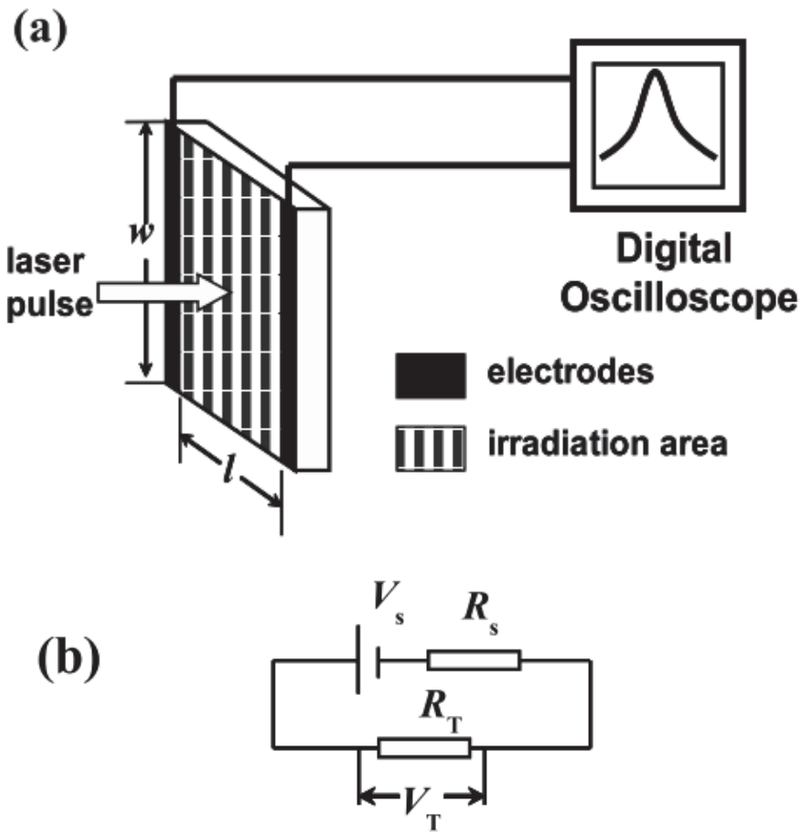

Fig. 5. (a) Schematic of the optical response measurement setup. l and w denote the length and width of the irradiated area, respectively. (b) Corresponding equivalent electrical scheme of the single crystal along the l direction. [12]

The suggested model for the source of the laser induced voltage in STO is fairly simplified, and only qualitatively explains the dependence of V_P on the irradiated width and length, as well as its dependence on the vicinal angles.

Picosecond photovoltaic effect has been observed in tilted Nb 0.7 wt %-$SrTiO_3$ (NSTO) single crystal under Nd:YAG pulse laser (a wavelength of 355 nm, a 25 ps duration, a 1 Hz repetition rate and an energy density of 1.07 mJ mm^{-2}) irradiation at ambient temperature without an applied bias.[23] The RT and FWHM are 828 and 670 ps, respectively.

In addition, ultrafast photoresponse were also observed in $LaSrAlO_4$ and MgO single crystals with their (001) planes tilted to the surface wafer at an angle of 10°.[24,25] When the samples were irradiated by 248 nm KrF laser pulses of 20 ns duration, open-circuit photovoltages were obtained. The RT and FWHM were ~10 ns and ~20 ns for tilted MgO and 6 ns and 19 ns for tilted $LaSrAlO_4$.

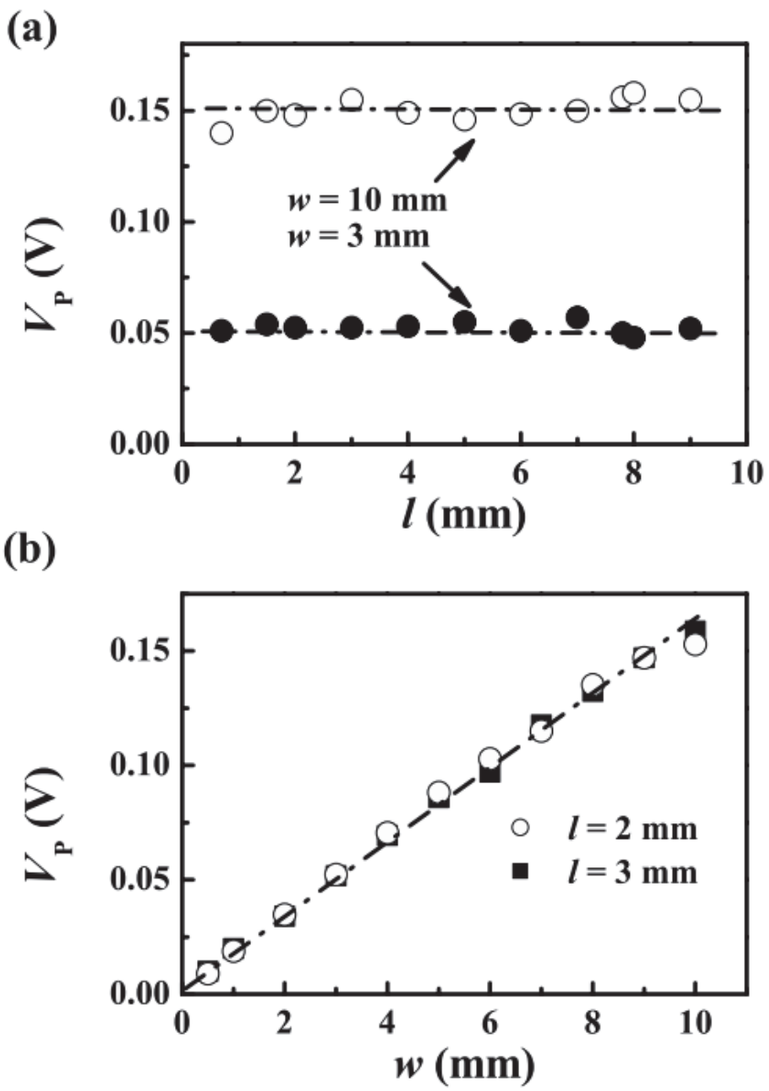

Fig. 6. The peak voltage V_P as a function of (a) length l and (b) width w of the irradiated area for 15° tilting angle. [12]

2.2 Thickness-dependent photovoltaic effects

The photovoltaic effects of tilted NSTO with different thicknesses were systematically investigated under the illuminations of ultraviolet pulsed lasers with the wavelength of 248 nm.[13] The as-supplied NSTO (001) (0.7 wt% Nb) single crystal wafer was investigated. The sample geometry is 5 × 5 mm^2 with a thickness of 0.5 mm and polished into several different

thicknesses mechanically (d = 120 ~ 460 μm). The wafer orientation is 10° tilted from the exact (100) orientation which was confirmed by an XRD measurement with the θ~2θ scan.
For the photovoltaic effect measurements, two Ag electrodes were applied and separated by 1 mm on the back of irradiated surface of the NSTO to avoid the photovoltaic effect due to contact barrier. Compex50 excimer pulsed laser with a laser spot of 5 × 13 mm^2, operating at a wavelength of 248 nm with 20 ns duration at a 2 Hz repetition rate, was used as the light source. The effective irradiation area is about 5 mm^2. The open-circuit photovoltaic signals were recorded using a digital oscilloscope terminated into 50 Ω.
Figure 7 shows the dependence of the peak photovoltaic signals (R_{VE}) on crystal thicknesses. With the decrease of thickness R_{VE} increased and reached to a maximum of 4.52 mV at 180 μm, which is ~2.63 times larger than that at 460 μm. However, R_{VE} decreased to 2.08 mV smaller than half maximum when the crystal is thinned from 180 μm to 120 μm. From the inset of Fig. 7, the R_{VE} linearly depended on the on-sample laser energy density E. Thus the thickness dependence of R_{VE} can be explained as following: there are many kinds of defects and traps (recombination centers) where the electrons and holes can locate in samples, owing to the doped 0.7 wt% Nb impurity, which is often found in single crystals and can be considered as carrier dilution effect. Only those carriers reaching to the electrodes in the back can be collected and give rise to photovoltaic signals. On one hand, with decrease of crystal thickness the amount of carriers collected by electrodes in the back increase due to lower loss, which is resulted from the shorter transport distances as well as less traps and recombination in thinner samples. Thus the photovoltaic signals for thinner samples are much larger than that for thicker samples. On the other hand, the decrease of thickness also leads to decrease of autologous carriers in NSTO single crystals, which limits the amount of carriers collected by electrodes. The competion between the above two factors results in a maximum photovoltaic signal.

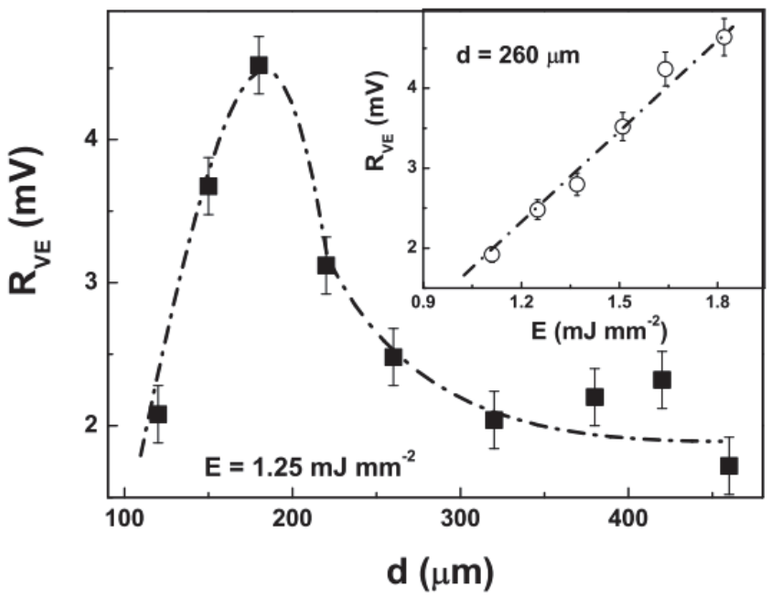

Fig. 7. Thickness and on-sample laser pulse energy density (inset) dependences of peak value responsivities of photovoltaic signals. [13]

Figure 8 shows the thickness dependence of the RT and FWHM of the photovoltaic signals. The response time is faster for the thinner sample. The differences of the RT and FWHM between the thickest and the thinnest crystals are about 4.49 ns and 9 ns, respectively. This dependence can be understood easily: the carriers induced by laser pulse were separated by lateral field in the NSTO single crystal, and traveled shorter distance to reach the electrodes for thinner samples so that faster photovoltaic responses can be observed.

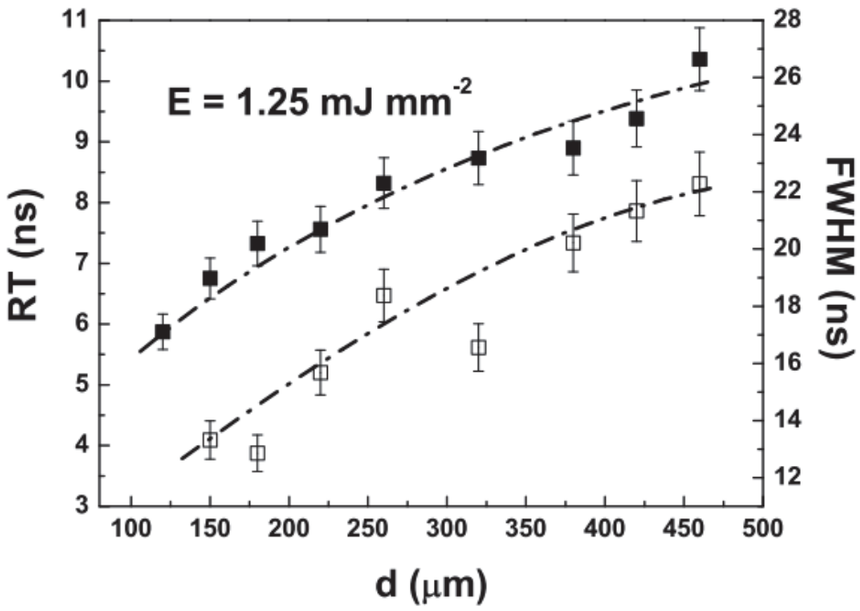

Fig. 8. Thickness dependence of RT (solid point) and FWHM (open point) of photovoltage. [13]

Experimental results show that the decrease in the crystal thickness is an effective method for improving the photovoltaic sensitivity in single crystals, suggesting the potential for optoelectronic detection applications.

2.3 Ultrafast photovoltaic effects in polar crystals

Silicon dioxide (SiO_2), which has good abrasion resistance, electrical insulation and high thermal stability, is widely used in electronics industry, refractory materials or glass production and so on.[26-28] Picosecond photovoltaic response has been observed in quartz single crystals under spectrally broadband laser irradiation from ultraviolet to near infrared without an applied bias at room temperature.

A mirror polished commercial quartz single crystal with 3 × 5 mm^2 in area, 0.5 mm in thickness (MTI Corporation Production, USA) and c-axis oriented (parallel to the normal of the illuminated surface) was used for the photoresponse studies. The samples have pure single crystal structures characterized by x-ray diffraction using Cu K_α radiation.

Figure 9 displays the temporal response of the open-circuit photovoltage responsivity R_{VE} equal to the photovoltage/on-sample-energy, and the primary photovoltaic signals are almost symmetrical. The inset of Fig. 9 displays the schematic circuit of the measurement. The Nd:YAG laser (pulse duration of 25 ps, repetition rate of 10 Hz) was used to irradiate the sample operating at the wavelengths of 1064, 532 and 355 nm. The photovoltaic signals

were recorded using a sampling oscilloscope terminating into 50 Ω. The RT and FWHM are about 465 and 586 ps, 403 and 570 ps and 419 and 720 ps for 1064 nm, 532 nm and 355 nm, respectively.

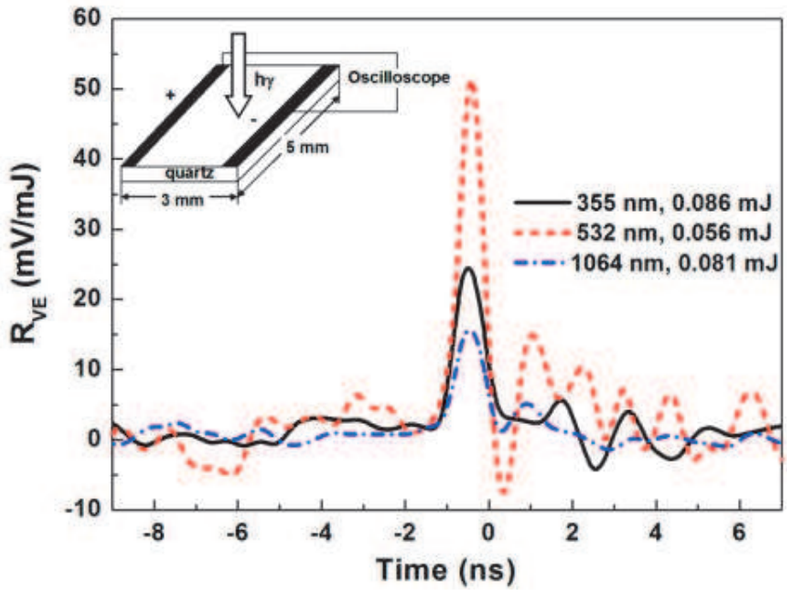

Fig. 9. Temporal response of a quartz single crystal under the irradiation of a Nd:YAG pulsed laser at room temperature without an applied bias. The inset displays the schematic circuit of the measurement. [14]

The peak amplitudes R^{P}_{VE} of R_{VE} as a function of the on-sample pulsed laser energy E_{in} are plotted in Fig. 10. It is found that the R^{P}_{VE} shows a high value when the sample was irradiated by a low energy pulse laser and drops gradually with the increase in E_{in}.

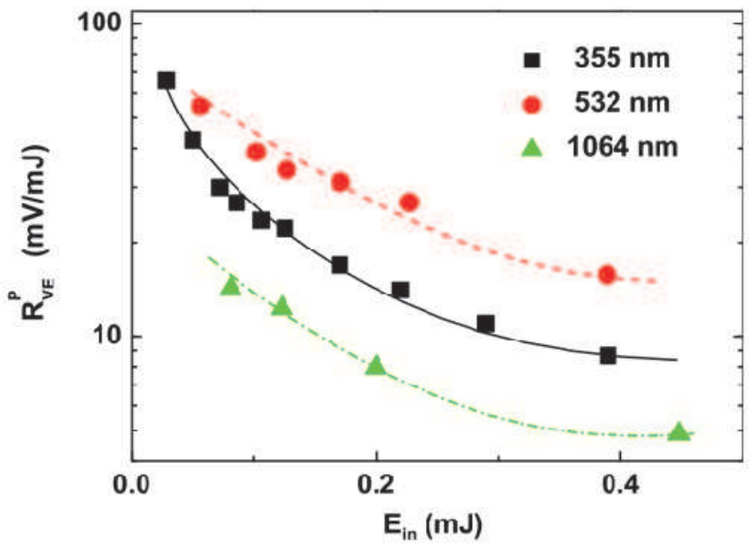

Fig. 10. Peak photovoltaic responsivity R^{P}_{VE} as a function of the on-sample laser pulse energy E_{in}. [14]

In addition, the samples were also illuminated directly by continuum solid state lasers (on-sample power: 20 mW) in the absence of an applied voltage at ambient temperature. The open-circuit photovoltaic signals were measured by a standard lock-in amplifier technique and recorded by a sampling oscilloscope terminating into 1 MΩ.
Figure 11 shows that the responsivity R_{VP}, equal to photovoltage/on-sample power, is about 0.476 μVmW^{-1}, 0.165 μVmW^{-1} and 0.188 μVmW^{-1} for 1064 nm, 808 nm and 532 nm, respectively, which resembles that under a bromine–tungsten lamp illumination (on-sample power: 1.08 mW). We also measured the picosecond laser-induced photovoltages in 10° tilting quartz single crystals and the signals were very close to those in the present nontilting samples, indicating that the Seebeck effect is ruled out.

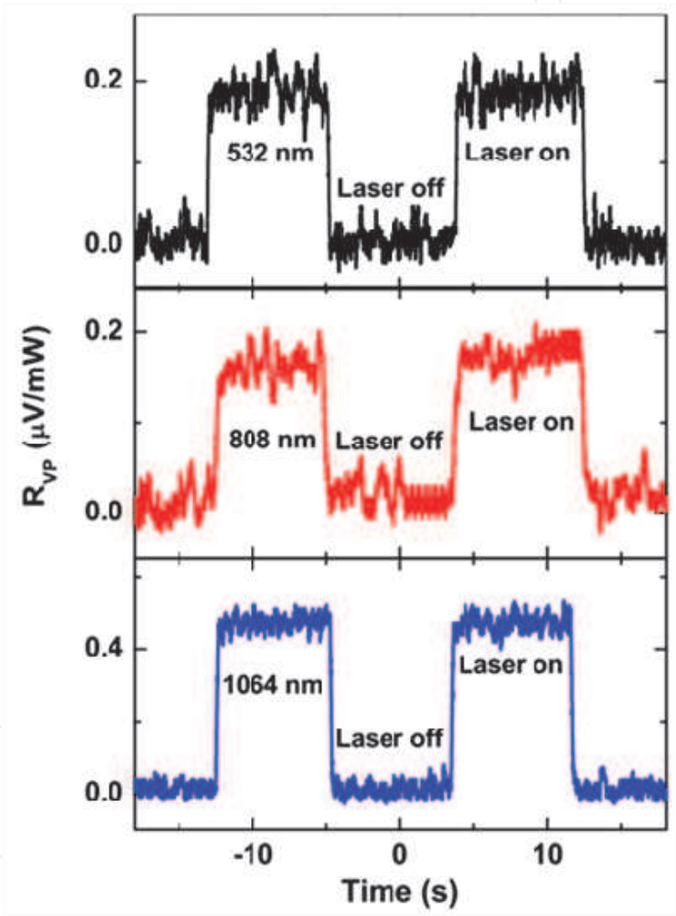

Fig. 11. Photovoltaic responsivity R_{VP} of a quartz single crystal under continuum laser illumination at room temperature without any bias. [14]

The present photovoltaic effect should relate to the trap centres existing in quartz single crystals. Based on metal–insulator contact theory,[29] the energy-band diagram for the interface between Ag and SiO_2 is shown in Fig. 12. The Fermi level (E_f) of Ag immediately after contact is higher than that of SiO_2. Thus, electrons will be transferred from the metal into SiO_2 to equalize the E_f. During the transmission, a portion of electrons are trapped by positively charged centres in the crystal and accumulated in traps. The contact potential

difference (C.P.D.) in the equilibrium state is estimated as ~0.64 eV, which is determined by the difference between the metal and insulator work functions. Under illumination a number of trapped electrons are freed into the conduction band (C.B.) of SiO_2 and removed by the built-in electric field. Eventually, photovoltage occurred in the present system. In this case, the trap level below the C.B. was estimated to be ~1.165 eV (1064 nm photon energy). From Fig. 9, the transient photovoltaic responsivities under picosecond irradiation are about 0.375 μVmW^{-1} and 1.31 × 10^{-6} μVmW^{-1} at 0.081 mJ and 0.056 mJ for 1064 nm and 532 nm, respectively, are about six orders of magnitude smaller than that under continuum light illumination. This indicates that the above factor cannot be responsible for the photovoltage under picosecond laser irradiation. In short-pulse materials processing, where the transient power density is very high (10^7-10^8 Wcm^{-2} in our case), it is necessary to consider such physical events as internal electron-lattice coupling, thermal transport or lattice distortion, etc. The laser radiation is first absorbed by the electrons within the ultrashort pulse duration and subsequently transferred to the crystal lattice through electron–phonon interactions over a characteristic time. In addition, the crystal structures of α-quartz (trigonal form) and β-quartz (hexagonal) do not give rise to pyroelectricity due to the symmetry of quartz. In contrast, the β_2 tridymite quartz with internal strains is a candidate for pyroelectric material owing to its lower symmetry and intricate structure.[30] Here, the secondary and tertiary pyroelectric effects, which are produced by deformation and inhomogeneous temperature distributions within the crystal, were introduced to meet our present results.

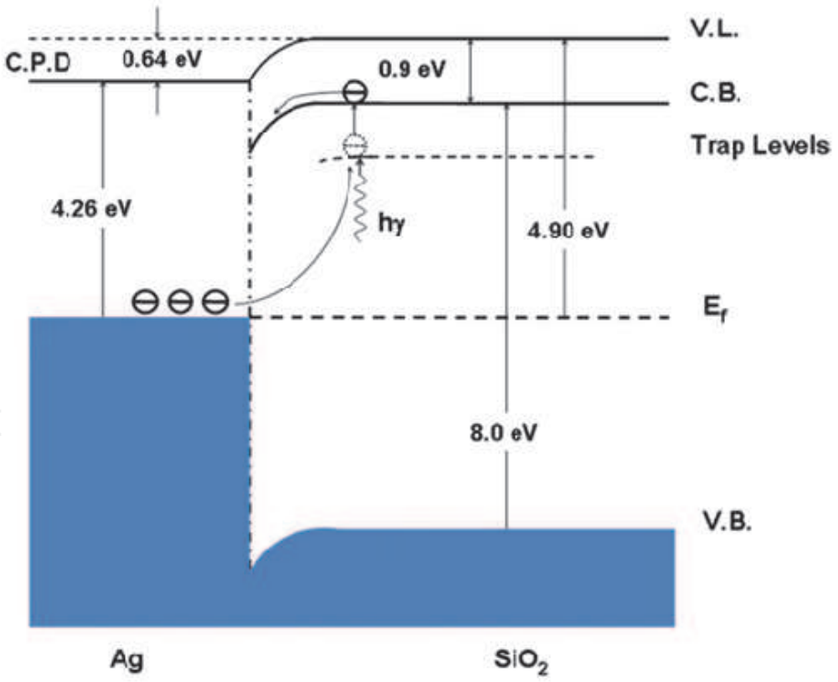

Fig. 12. The schematic band structure of the Ag–SiO_2 contact. C.P.D., V.L., C.B., V.B. and Ef denoted the contact potential difference, vacuum level, conduction band, valence band and Fermi level, respectively. [14]

From the heat flow equation $Q = \kappa \nabla T \approx \gamma E_{in}/\tau$, where Q is the heat current density, $\gamma \approx 1\%$ the absorption coefficient, $\kappa \approx 1.38$ $Wm^{-1}K^{-1}$ the thermal conductivity and τ the response

time. With these values, the surface temperature can be estimated to be about 2×10^4 K when the sample is irradiated by a picosecond pulse laser. So the β_2 tridymite structure can be formed in crystals since the surface temperature is much higher than the transition temperature of 1143 K from β-quartz to β2 tridymite phases.[31] And also a non-uniform transient temperature distribution is induced on the crystal surface due to Gaussian intensity distribution of the laser pulse. Thus, non-uniform stress and strain distributions were created around the irradiated region as shown in Fig. 13.[32] Due to the pyroelectric effect of β_2 tridymite quartz, the positive and negative charge centres are separated slightly, leading to polarization (Fig. 13(c)), and eventually lateral photovoltage signals are observed.

Typical lateral ultrafast signals have also been observed in $LiNbO_3$ single crystals under Nd:YAG laser (pulse duration of 25 ps, repetition rate of 10 Hz) irradiation. The RT and FWHM are about 1.5 ns and 1~2 ns. Under the laser irradiation, photo-induced carriers are separated and assembled at the two electrodes by the spontaneous polarisation electric field.

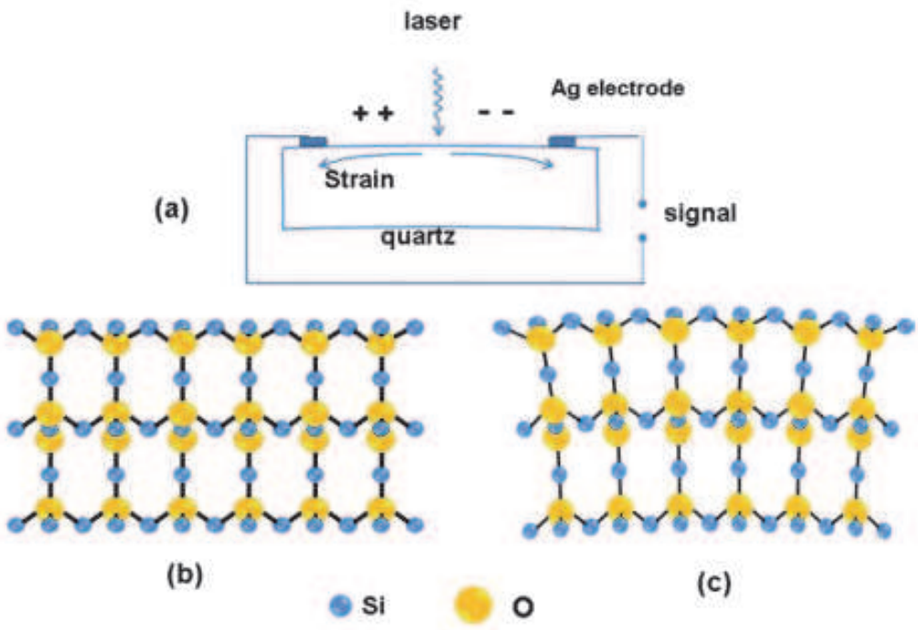

Fig. 13. (a) Diagram illustrating the sample structure. (b) and (c) are the β_2 tridymite structures before and after laser irradiation, respectively. [14]

3. Ultrafast photoresponse and its tunable effects in oxide films

3.1 Ultrafast photoresponse in oxide films

Recently, many researches have devoted to exploring photovoltaic properties and verifying new device concepts based on doped manganite thin films and heterostructures.[33-36] Technological interest has centered on solar cells, light-emitting diodes, and photoelectric detectors.[37,38] Previous researches showed that these materials represent good properties, such as ultrafast response, high-sensitivity, broad-spectrum and position-sensitivity, as optoelectronic device materials.

The $La_{1-x}Ca_xMnO_3$ (LCMO) thin films were deposited on several kinds of substrates (Si; $LaSrAlO_4$; MgO; NSTO) by facing-target sputtering technique.[39] The substrate temperature was kept at 680 °C and the oxygen partial pressure of 30 mTorr during deposition. The film thickness is uniform, controlled by sputtering time with the deposition rate (~0.03 nm/s). After the deposition, the vacuum chamber was immediately back-filled with 1 atm oxygen gas to improve the oxygen stoichiometry. Then, the samples were then cooled to room temperature with the substrate heater power cutting off.

In tilted LCMO films, picosecond ultrafast photoresponse were observed. The structure of the $La_{2/3}Ca_{1/3}MnO_3$/MgO sample characterized by XRD and transmission electron microscopy (TEM) shows that the $La_{2/3}Ca_{1/3}MnO_3$ film is a single phase and epitaxial growth. The sample of 5×5 mm² geometry has been used for the photoelectric properties measurement under the 355 nm Nd:YAG laser irradiation with 25 ps duration at a 2 Hz repetition. The waveforms were recorded by a sampling oscilloscope terminated into 50 Ω. Figure 14 displays the temporal waveform of the open-circuit photovoltage. The RT and FWHM are about 224 and 574 ps.

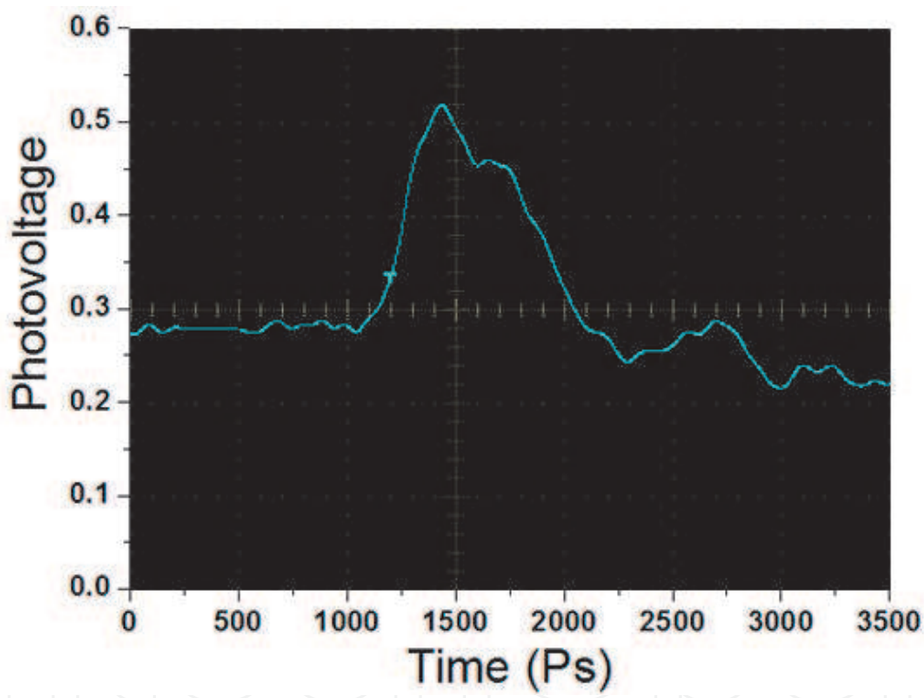

Fig. 14. The open-circuit photovoltaic waveform of $La_{2/3}Ca_{1/3}MnO_3$/MgO sample irradiated by a 355 nm laser pulse of 25 ps duration.

ZnO is a promising short-wavelength optoelectronic material because of its direct wide band gap (3.37 eV at 27 K), large exciton binding energy (60 meV) and high transparency (>80%) in the visible wavelength region. Over the past years a great deal of physical properties has been investigated in doping ZnO thin films. Lim et al. reported the fabrication of ZnO based LEDs using sputter deposited P-doped ZnO as the p-type layer.[40] Ye et al. used N–Al codoping for p-type doping and fabricated ZnO LEDs on Si with sputter deposition.[41] Myong et al. obtained highly conductive Al-doped ZnO thin films.[42] Ataev et al. reported a resistivity of 1.2×10^{-4} Ωcm for Ga-doped ZnO thin films

grown by chemical-vapor deposition.[43] The UV photovoltaic response of Ag-doped ZnO thin films deposited at different temperature has been studied.[44]
The films were prepared on fused quartz substrates by pulsed laser deposition (PLD). A KrF excimer laser (wavelength: 248 nm, pulse width: 30 ns, energy density: 1 J/cm^2) was used for ablation of a ZnO mosaic target (1/4 area of the target was uniformly covered with high-purity silver slices in the shape of a sector). In our experiment, the repetitive frequency of the laser was 4 Hz, the O_2 pressure was 5×10^{-4} Pa, and the temperature of the substrates varied from 350 to 550 ^oC. All the samples were cooled to room temperature under an O_2 pressure of 5×10^{-4} Pa in the chamber.

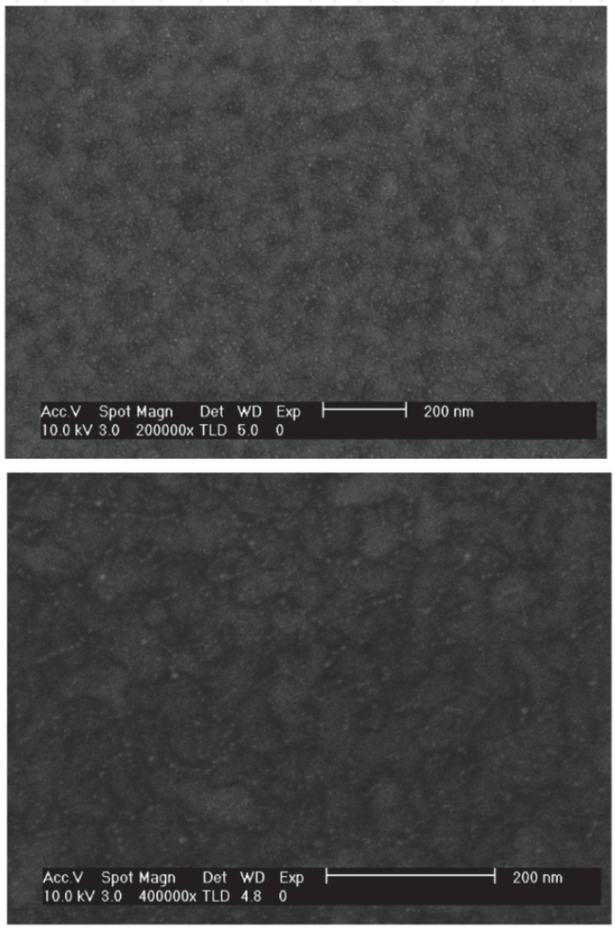

Fig. 15. SEM morphologies of Ag-doped ZnO films deposited at (a) 350 °C and (b) 550 °C. [44]

Figs. 15(a) and 15(b) show the SEM morphologies of Ag-doped ZnO films deposited at 350 and 550 ^oC, which is different from that at 450 ^oC reported in Ref. [45]. From the SEM image the Ag-doped ZnO films consist of grains separated by grain boundary (GB), and Ag would preferentially choose to sit in vicinity of grain boundaries due to its large ionic radius.
For the photovoltaic measurements a Nd:YAG laser (wavelength 266 nm) was used as the light source with a pulse energy of 1 mJ and a light spot of 6 mm in diameter. The photovoltaic signals were monitored with a 500 MHz oscilloscope terminated into 50 Ω.

Under the same condition, the 308 nm excimer laser was adopted to irradiate the samples. Fig. 16 presents typical open-circuit photovoltages transient of Ag-doped ZnO films deposited at different temperature (350 ^{o}C, 450 ^{o}C and 550 ^{o}C). Under pulsed 266 nm laser irradiation of 25 ps duration, the photovoltaic signals had FWHMs of 0.9, 0.8 and 1.0 ns, limited by the oscilloscope and peak photovoltages of 29, 72 and 28 mV for 350, 450 and 550 ^{o}C, respectively. Furthermore, Fig. 16(d) shows the temporal response of the Ag-doped ZnO film to a 20 ns 308 nm laser pulse. The peak photovoltage reaches ~29 mV. The FWHM and RT are ~20 and ~10 ns, respectively, which are limited by the excitation laser.

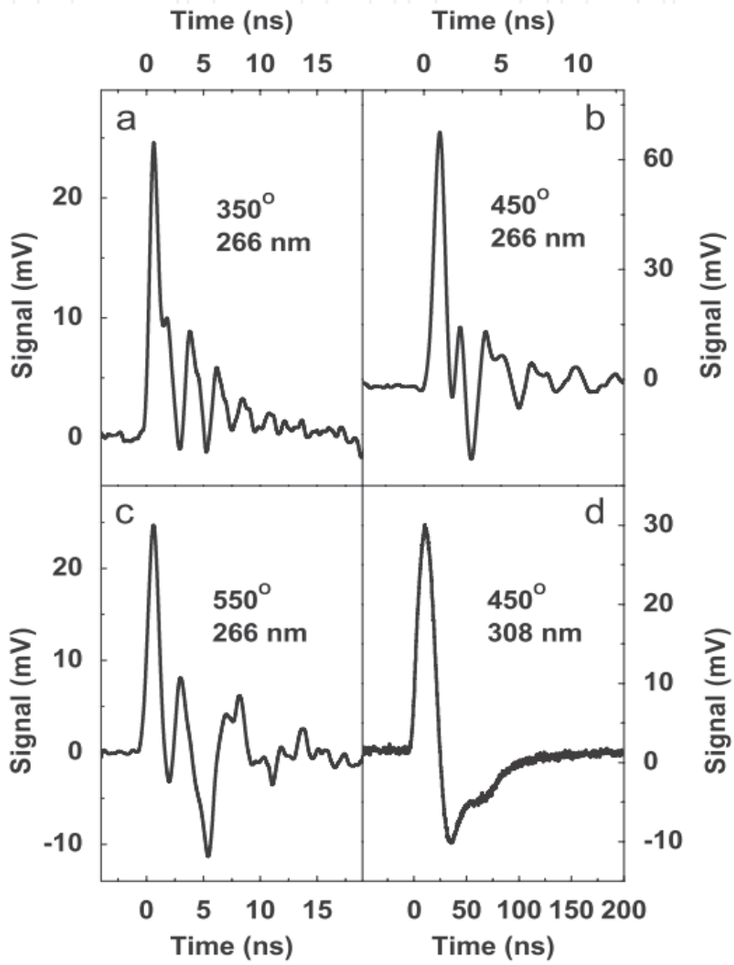

Fig. 16. Open-circuit photovoltages of Ag-doped ZnO films deposited at (a) 350 ^{o}C, (b) 450 ^{o}C and (c) 550 ^{o}C under the excitation of 266 nm laser. (d) Shows the photovoltage of the sample deposited at 450 ^{o}C under the excitation of 308 nm laser. [44]

We also studied the photovoltaic effect of ZnO films without Ag under the same condition and no voltaic signal appeared in our oscilloscope, indicating that Ag clusters in vicinity of grain boundaries play an important role in the present photovoltaic characteristics. Thus, a simplified model can be given on the origin of the photovoltaic signal. There is a chemical potential shift $\Delta\mu$ between the GB region and the grain, which might induce a depletion layer in the GB region and the build-in voltage V_b is given by $\Delta\mu$, $V_b = \Delta\mu$. Shu-Ting Kuo et

al. calculated the electrostatic barrier of one-grain boundary of Ag-doped ZnO was approximately 2 V.[46] When the laser irridiates the sample, electron-hole pairs can be excited in the grains and GB regions since an energy gap of ZnO between occupied and empty electronic states is smaller than UV photon energies (4.0 eV for 308 nm and 4.7 eV for 266 nm). And then the nonequilibrium carriers are separated by the built-in electric field near the GB, eventually, leading to the appearance of an instant photovoltage.

Since the sample is polycrystalline, there should be an equal number of grains with photogenerated carriers shifting in one direction as in the opposite direction; hence there should be not net current flow and no photovoltage signal. This is not the case. In fact, it is uncertain why there is an overall preferred direction for the flow of the photo-generated current. This behavior may be due to the asymmetry of the lattice which induces an asymmetric moving of the excited carriers in a preferred direction. Further study on the nature of the photovoltaic properties of such a system is under way.

4. External field tunable effects

Perovskite-type manganites have attracted a great deal of interest because of the versatile electronic states that can be controlled by various kinds of external perturbations.[47-49] Photoexcitation offers an attractive method to vary the concentration of charge carriers without the added complication of a change in the chemical composition and the crystal structure.

The voltage tunable photodetecting properties have been studied in a $La_{0.6}Ca_{0.4}MnO_3$ film grown on 10° tilted LSAO (001) substrates under ultraviolet pulsed laser (248 nm; 20 ns) irradiation.[15] The photovoltaic effect of the $La_{0.6}Ca_{0.4}MnO_3$ thin film on 10° tilted LSAO substrate was measured under different bias at room temperature, and the open-circuit photovoltage transient V_R, across the input impedance of oscilloscope and recorded by oscilloscope, is displayed in Fig. 17(a). The RT and FWHM are about 12 and 23 ns, respectively. The V_R^b in Fig. 17(a) denotes the baseline recorded by the oscilloscope for laser-off state, which was caused by the external bias and the input impedance, and shifts from -0.69 to 0.69V symmetrically for V^b from -20 to 20 V. The photoinduced voltage V^P defined by $V^P=V_R^P-V_R^b$ is plotted in Fig. 17 (b) as a function of the applied bias V^b, and increases from 0.69 to 1.85 V with V^b from -20 to +20 V.

A 0.2 Ω resistance was connected in parallel with the sample (see the up inset of Fig. 18 (a)) for further studying the electric tunable photocurrent responses of the $La_{0.6}Ca_{0.4}MnO_3$ films. It is found that the baseline V_R^b recorded by the oscilloscope did not change due to the very small connected resistance (Fig. 18(a)), and RT is reduced to about 4 ns. The tail traces of the waveforms show some periodic oscillations persisting for tens ns which may be due to the signal reflection arising from an impedance mismatch in the circuit. The peak photocurrent I_{AB} was calculated by $I_{AB} \approx V_R^P/0.2\ \Omega$ where V_R^P is the peak voltage across the connected resistance 0.2 Ω, and increased monotonically to 0.74 A at V^b = 20 V (Fig. 18(b)), which is 1.82 times higher than 0.41 A at V^b = -20 V.

From the cross-sectional TEM image of $La_{0.6}Ca_{0.4}MnO_3$/LSAO (Fig. 19(a)) the film thickness was fairly uniform and about 120 nm. No appreciable interdiffusion occurred and no evidence of secondary phases was observed from the high resolution TEM (HRTEM) picture at the $La_{0.6}Ca_{0.4}MnO_3$/LSAO interface (Fig. 19(b)), which is agreement with the XRD investigations. Due to the 10° tilted substrate, the $La_{0.6}Ca_{0.4}MnO_3$/LSAO interface is not a

plane and a terrace structure occurs, which is labeled in Fig. 19(b). This denotes that we have obtained exactly epitaxial the 10° tilted thin films, and the terrace structure is an important factor for the present photodetecting properties.

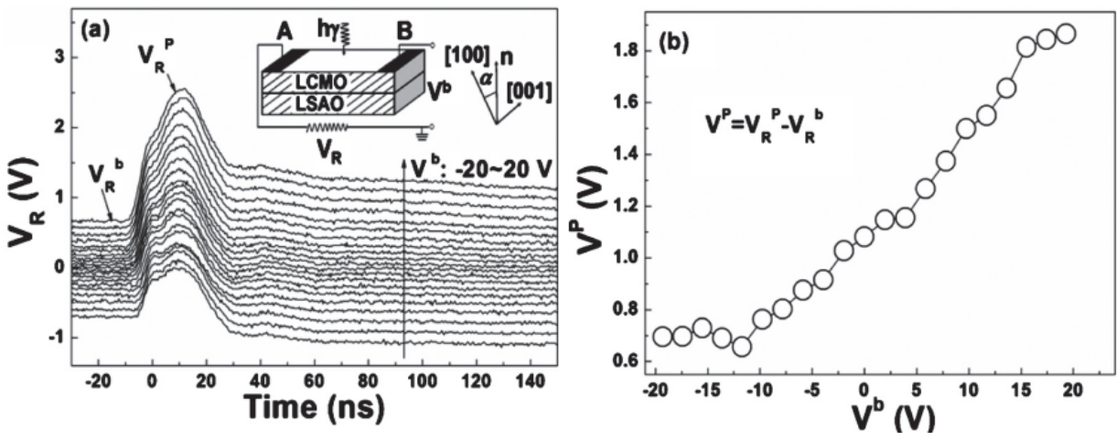

Fig. 17. (a) The photovoltaic pulses for $La_{0.6}Ca_{0.4}MnO_3$/LSAO under the illumination of a 248 nm laser at different biases recorded by an oscilloscope with an input impedance of 50. The inset displays the schematic circuit of the measurement. (b) The photoinduced voltage V^P defined by $V^P = V_R^P - V_R^b$ as a function of the applied bias V^b. The inset shows that V_R^P as a function of the applied bias V^b. [15]

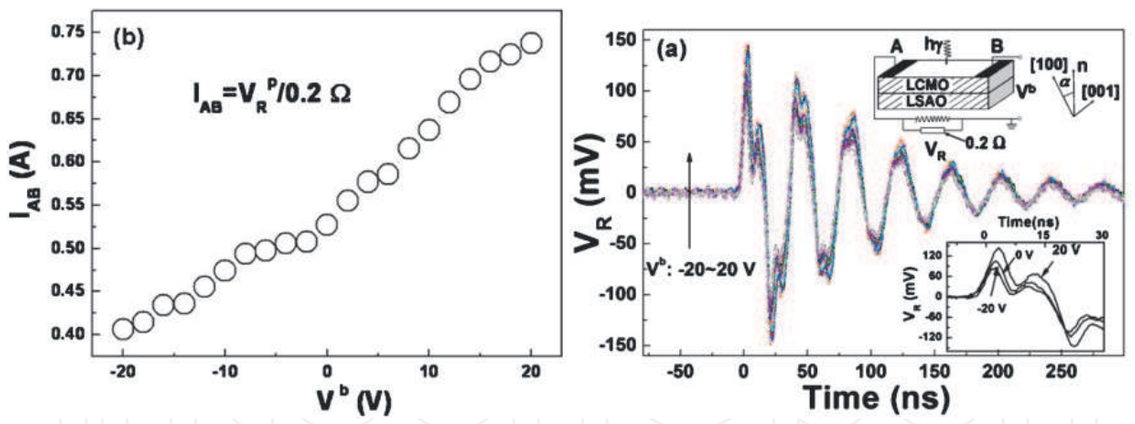

Fig. 18. (Color online) (a) The photovoltaic pulses and (b) peak photocurrent for $La_{0.6}Ca_{0.4}MnO_3$/LSAO under the illumination of a 248 nm laser at different biases recorded by an oscilloscope with a parallel resistance of 0.2 Ω. [15]

Because of the terrace structure in the interface of the $La_{0.6}Ca_{0.4}MnO_3$/LSAO, which is caused by the tilted angle of the substrate and clearly shown in the TEM image (Fig. 19(b)), we depicted schematic drawing under the irradiation of the pulsed laser as shown in Fig. 20. If the laser is divided into two components of being parallel and perpendicular to the tilting direction, the transient carrier density along each axis is proportional to the illuminated power perpendicular to the tilting direction. And the ratio between the irradiation intensities on (010) and (001) faces can be denoted as $I_{010}/I_{001}=\cos\alpha/\sin\alpha\approx5.67$ for α = 10°, so

as the carries density. Since the photon energy of 248 nm wavelength (4.86 eV) is above the band gap of $La_{0.6}Ca_{0.4}MnO_3$ (~1.2 eV), electron-hole pairs are generated in the $La_{0.6}Ca_{0.4}MnO_3$ film, therefore, a gradient of carrier density was generated along the lateral orientation. In our case, the laser we used is a 248 nm KrF excite laser beam with an energy density of 0.31mJ/mm² in duration of 20 ns, so the amount of laser induced carriers should be comparable with or even much larger than that of the majority carriers in the $La_{0.6}Ca_{0.4}MnO_3$; on the other hand, there exists no built-in field which exists in the p-n junction to separate holes and electrons. Therefore, both the electrons and holes play an important in the photovoltaic, and a mechanism based on the difference between the mobilities of electrons and holes, such as Dember effect, was proposed to explain the photovoltaic effect in $La_{0.6}Ca_{0.4}MnO_3$/LSAO.

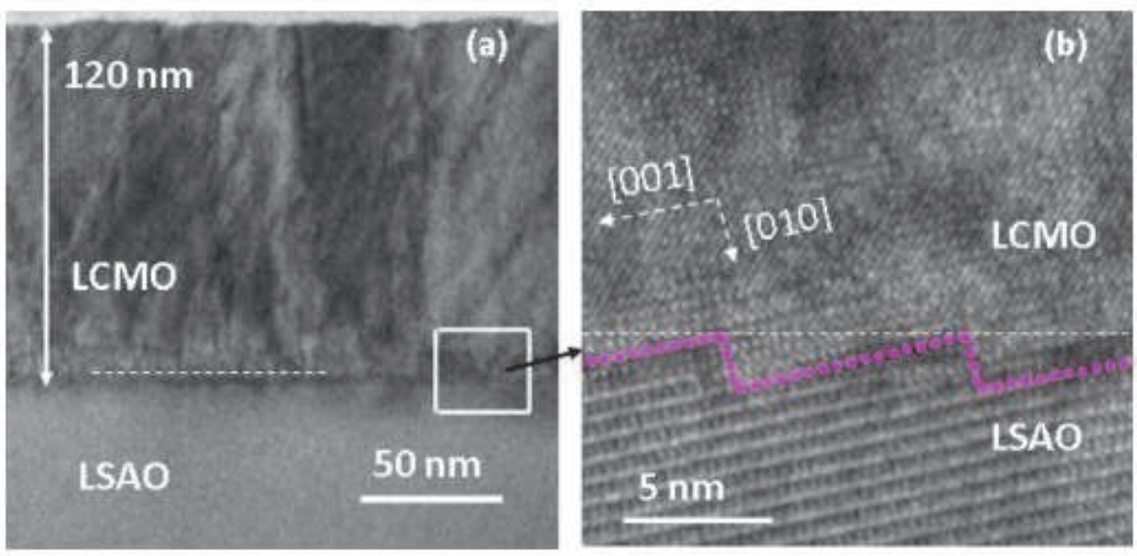

Fig. 19. (Color online) Cross-sectional TEM images of (a) LCMO/LSAO sample and (b) LSMO/LSAO interface. The dashed lines denote the interface position. [15]

Due to the applied bias and Dember effect (because of the difference of coefficient of diffusion between holes and electrons), an electric filed $E=E_b+E_d$ was generated where E_b and E_d denote the electric filed generated by applied bias and Dember effect, respectively. The drift current density j is presented as $j = j_p + j_n = n_p q v_p - n_n q v_n$, where j_p and j_n are the current density of the holes and electrons, n_p, v_p and n_n, v_n are the density, drift velocity of the holes and electrons, respectively, q is the unit of charge. Take electron as an example, we can obtain that $v_n(t) = v_{n0} - q/m_n^* Et$, where v_{n0} denotes the average velocity of the electrons after the scattering and should be 0 due to the random of the scattering, m_n^* is the effective mass of electron, E is the electric filed, and t is the average time between two scattering which can be denotes as relaxation time τ. Thus $v_n = -q/m_n^* \tau E$. Therefore, the drift carry density can be presented as $j = (\mu_p - \mu_n) E$, where $\mu_p = q/m_p^* \tau$ and $\mu_n = q/m_n^* \tau$ present the mobility of the hole and electron. When the applied bias is positive or negative, $E_b > 0$ or $E_b < 0$, therefore, the photovoltage is enhanced or reduced.

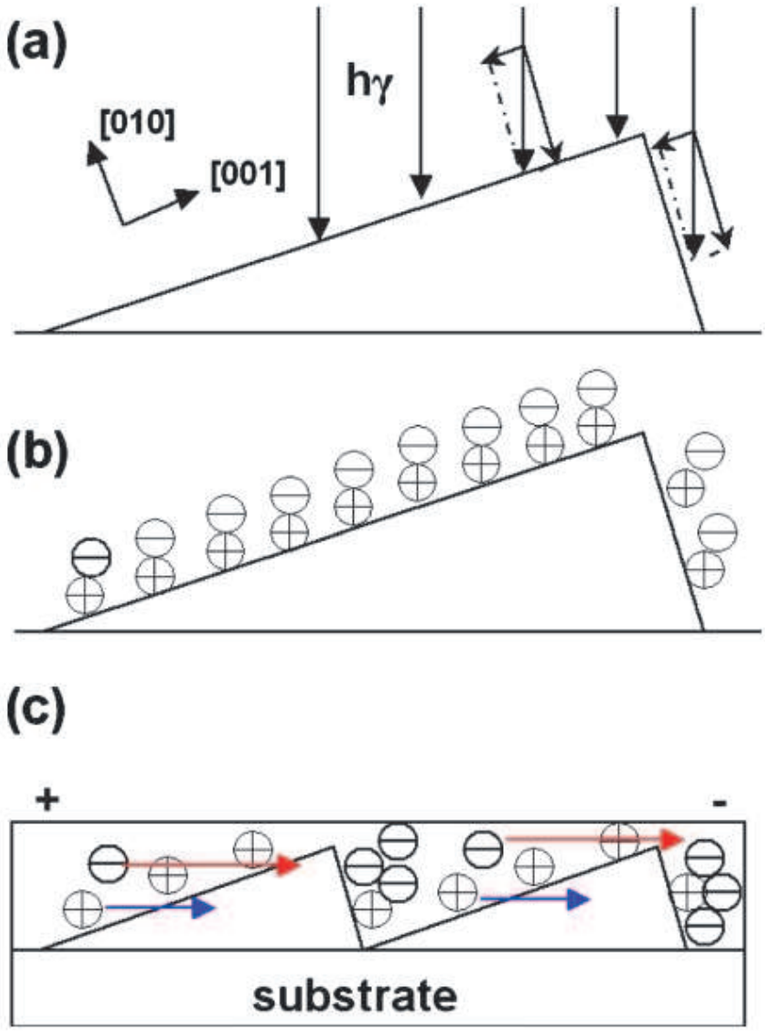

Fig. 20. (Color online) (a) The schematic drawing under the irradiation. (b) The difference of the carry destiny caused by the miscut angle. (c) The transient movement of the photogenerated carriers of the $La_{0.6}Ca_{0.4}MnO_3$. [15]

The enhanced magnetoresistance (MR) effect has been discovered under laser illumination in the $La_{2/3}Ca_{1/3}MnO_3$ film on the n-Si substrate at room temperature.[16]

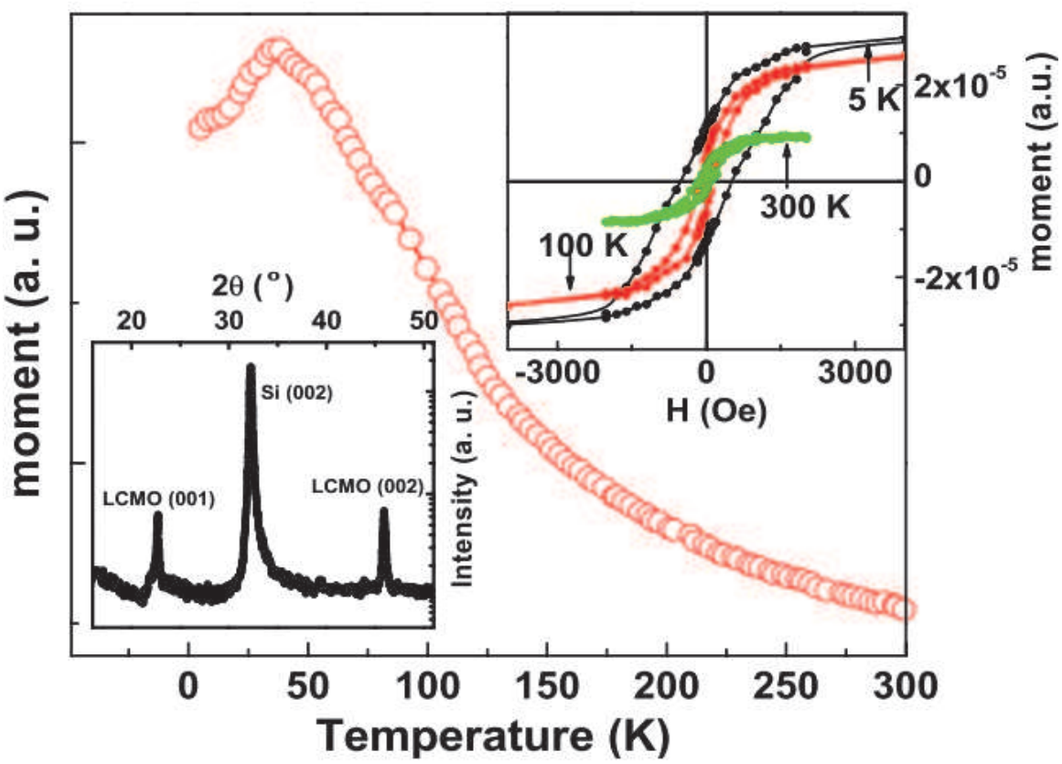

Fig. 21. The magnetic moment as a function of temperature of the junction. The left and right insets show the XRD pattern and magnetic hysteresis loop, respectively. [16]

XRD spectrum confirmed that the $La_{2/3}Ca_{1/3}MnO_3$ layers were oriented along the Si [001] direction as shown in the left inset of Fig. 21. The temperature dependence of magnetic moment was performed with SQUID. The magnetic hysteresis loop at room temperature shows a magnetic coercivity of 80 Oe in the right inset of Fig. 21, which reveals the existence of a few ferromagnetic phases near room temperature in the $La_{2/3}Ca_{1/3}MnO_3$ layer due to the phase separation scenario.[50] Accordingly, it is reasonable to infer the small MR in the junction at room temperature. From the TEM image of the heterojunction in Fig. 22, it is clear that the $La_{2/3}Ca_{1/3}MnO_3$ nano columns (LCMO2) are well crystallized with a single-phase perovskite structure. There is also an about 20 nm thick $La_{2/3}Ca_{1/3}MnO_3$ layer (LCMO1) on the surface of SiO_2, which could be due to interdiffusion. The lattice images can be clearly seen in the LCMO2 layer in Fig. 22(b). The atomically sharp interface between the SiO_2 and Si substrate was also observed in Fig. 22(c).

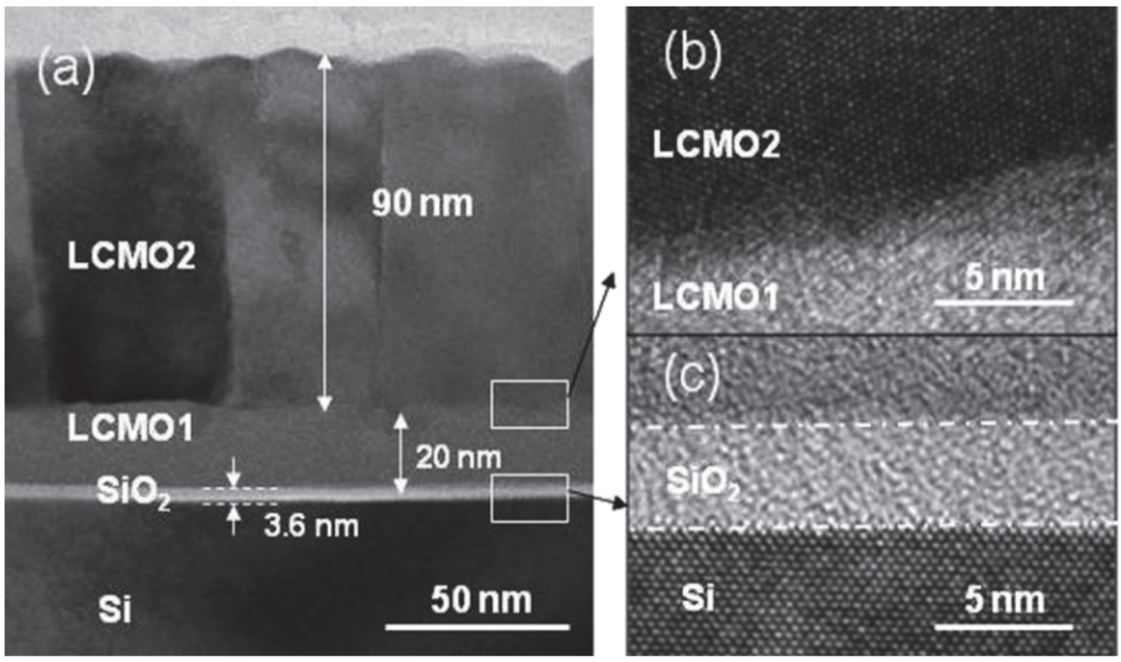

Fig. 22. A cross-section TEM image of the heterostructure. The SiO_2 layer can be clearly seen between the $La_{2/3}Ca_{1/3}MnO_3$ and Si substrate. [16]

The I-V characteristics of the junction were shown in Fig. 23 in different magnetic fields (H = 0, 1.81, 5.51 kOe) with and without laser irradiation. I+, V+, I- and V- are the four probes for the I-V measurement, and present current anode, voltage anode, current cathode and voltage cathode, respectively. The slope of the I-V curves becomes steeper and the junction current increases when irradiated by the laser in the reverse-bias case (bias current flows from Si substrate to $La_{2/3}Ca_{1/3}MnO_3$ film), which presents a decrease in junction resistance. This originates from the increased amount of the carriers due to light illumination. A great modification of resistance due to magnetic field was observed. At a reverse-bias current of -200 μA the output voltages change from -2.52 V to -2.46 V and -2.55 V in the selected fields of 1.81 kOe and 5.51 kOe, respectively. This effect is more striking under laser irradiation. For instance, the output voltages change from -1.88 to -1.84 and -2.10 V in 1.81 and 5.51 kOe under a bias of -200 μA when the junction is irradiated by laser.

Figure 24 reviews the dependence of MR on bias current in different magnetic fields, which were applied perpendicularly to the interface of the junction as shown in the inset of Fig. 24. The MR values become nearly constant under larger reverse bias current. When the junction was irradiated with a laser under reverse bias current, the MR values dramatically increase and are positive in larger magnetic field like 3.38 and 5.51 kOe. The ΔMR, defined as MR (laser on)—MR (laser off) for a fixed H, is larger under reverse current than under forward current as shown in the inset of Fig. 24.

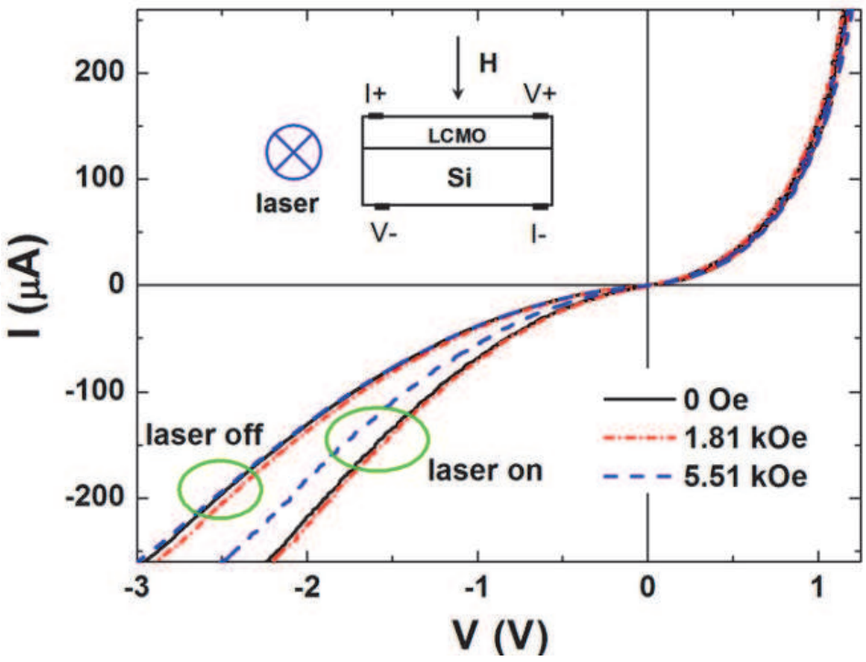

Fig. 23. I-V characteristics of the junction measured by tuning bias current in 0, 1.81 and 5.51 kOe at room temperature under 808 nm laser illumination on the interface. The inset shows the schematic measurement of I-V. The H was perpendicular to the junction interface and laser irradiation direction which was parallel. [16]

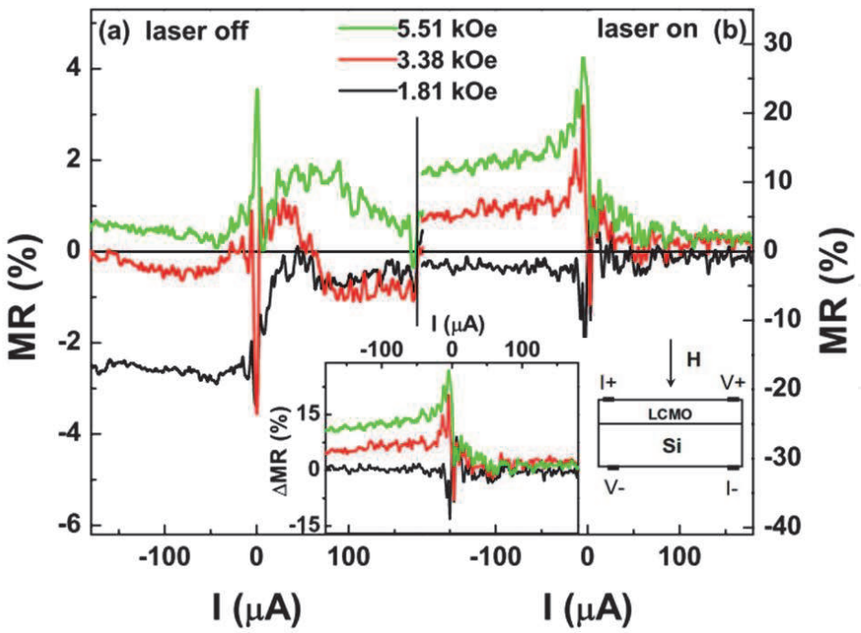

Fig. 24. The dependence of MR values of the junction on bias current in 1.81, 3.38 and 5.51 kOe at room temperature. The inset shows the dependence of ΔMR on bias current. [16]

Figure 25 shows the dependence of MR of the junction in magnetic field. The MR values increase and have a crossover from negative to positive values with increasing magnetic field H, which is different from the negative MR of the $La_{2/3}Ca_{1/3}MnO_3$ compound family. The MR values dramatically increase from 0.54% to 18% and 0.15% to 13% under -39 and -99 μA reverse-bias currents in 6.4 kOe, respectively, when the junction is irradiated by laser. This result demonstrates the possibility to gain great MR values in a broad temperature range by irradiating perovskite-type oxide heterojunction.

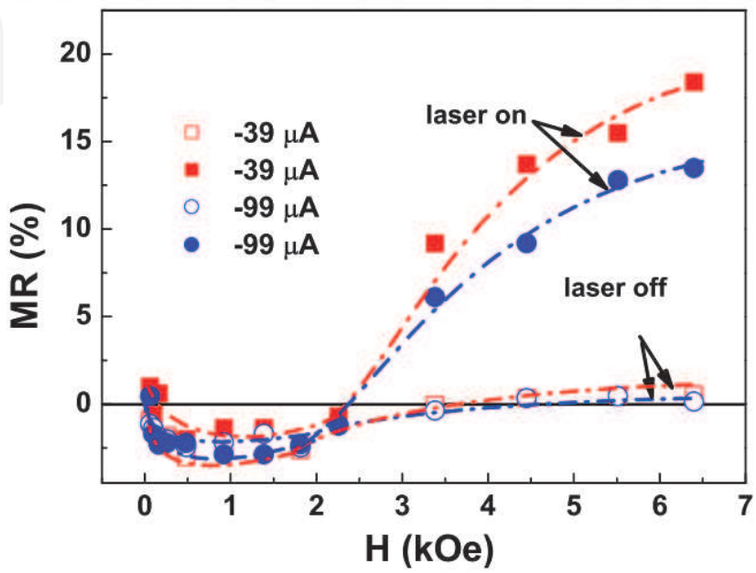

Fig. 25. The dependence of MR values on H under -39 and -99 μA with and without laser illumination in the junction at room temperature. [16]

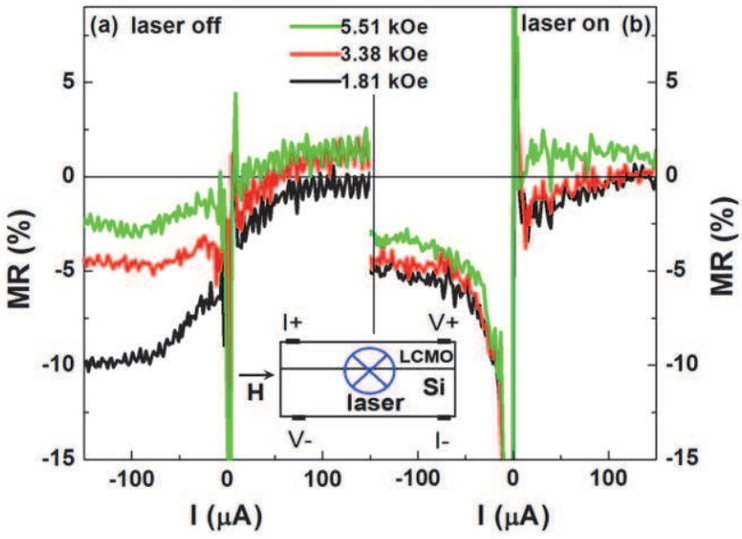

Fig. 26. The dependence of MR values of the junction on bias current in 1.81, 3.38 and 5.51 kOe fields at room temperature. The H was parallel to the junction interface and perpendicular to the direction of light which was parallel to the junction interface. [16]

In addition, when the H was applied parallel to the junction interface, the photo-induced enhanced MR effect has also been discovered at room temperature. As shown in Fig. 26, the MR ratios increase from -6.7%, -3.5% and -1.5% to -9.1%, -8.9% and -8.0% under -25 μA reverse- bias currents in 1.81 kOe, 3.38 kOe and 5.51 kOe, respectively, when the junction is irradiated by a 808 nm cw laser.

The high resolution TEM confirmed a native oxide (SiO_2) layer on the Si surface. Thus the junction can be treated as the $La_{2/3}Ca_{1/3}MnO_3/SiO_2/Si$ heterojunction. The photon energy (about 1.54 eV) of 808 nm laser is larger than the band gap of Si (about 1.12 eV) and $La_{2/3}Ca_{1/3}MnO_3$ (about 1 eV). When the laser directly irradiates onto the $La_{2/3}Ca_{1/3}MnO_3/SiO_2/Si$ interface, electrons in the valence bands (VB) of both $La_{2/3}Ca_{1/3}MnO_3$ and Si absorb photons and make a transition into the conduction bands (CB), generating electron–hole pairs. As indicated above, the ultrathin native SiO_2 oxide layer exhibits the large potential barrier, resulting in a large junction resistance.

When bias currents are applied, the carriers get energy to hop into the trap energy levels formed by defects in the SiO_2 insulator and are trapped in these levels leading to space charge [51]. It is easier for the charge carriers to tunnel through the SiO_2 space charge region than surmount the interfacial barrier. These tunnelling carriers form tunnelling current. The orbital motion and mobility reduction of the tunnelling charge carriers caused by the Lorentz force in magnetic field will depress tunnelling current and increase MR [52]. But the amplitude is relatively small. On the other hand, there was a ferromagnetic phase in $La_{2/3}Ca_{1/3}MnO_3$ at room temperature, which can lead to anisotropic MR (AMR) [53]. The intrinsic origin of AMR is the spin-orbit coupling and a larger probability of s–d scattering of electrons in the direction of magnetic field [54]. It is positive and grows with the applied magnetic field when the magnetic field is parallel to the current and negative when perpendicular [55, 56].

The present system under investigation consists of a photo-activated junction of manganite/oxide/n-Si and therefore the MR arising from this junction is tunnelling AMR (TAMR), because there is only one magnetic electrode. When the junction interface is illuminated by laser by side, great numbers of carriers are generated in both $La_{2/3}Ca_{1/3}MnO_3$ and Si side, which enhance tunnelling current and it can be seen from Fig. 23 that the I-V curves become steeper under laser illumination. When a negative bias current is applied, photogenerated electrons (with spin polarization) from $La_{2/3}Ca_{1/3}MnO_3$ contribute partly to tunnelling current. As the tunneling current is nearly parallel to applied magnetic field (the case in Fig. 23), TAMR is positive. As confirmed in Fig. 25, the TAMR will be enhanced when the magnetic field is perpendicular to tunnelling current. If a positive bias (from Si to $La_{2/3}Ca_{1/3}MnO_3$) is applied on the sample, there are no polarized carriers and no tunnelling current through the junction in the system. Thus the change of MR was small when positive currents were applied as shown in Fig. 24 and Fig. 26.

5. Conclusion

In conclusion, the characteristics of ultrafast photoresponses in oxide single crystals and films have been investigated. The RT and FWHM of the photovoltage signals were measured. Picosecond and nanosecond photoresponses were observed in tilted perovskite oxides (STO, NSTO and $LaSrAlO_4$), polar crystals (SiO_2 and $LiNbO_3$), tilted manganite films ($La_{1-x}Ca_xMnO_3/LaSrAlO_4$ and $La_{1-x}Ca_xMnO_3/MgO$) and Ag-doped ZnO films. Theoretical investigations about interesting experimental phenomena are presented. External field

tunable effects for the photovoltaic effect were also systematically studied. Experimental results reveal the potential for optoelectronic detection applications.

6. Acknowledgement

This work was supported by the Program for NCET, NSFC, RFDP, Foresight Fund Program from China University of Petroleum (Beijing).

7. References

[1] M. Razeghi and A. Rogalski, J. Appl. Phys. 79, 7433 (1996).
[2] M. Topic, Appl. Phys. Lett. 78, 2387 (2001).
[3] J. W. Tomm, B. Ullrich, X. G. Qiu, Y. Segawa, A. Ohtomo, M. Kawasaki, and H. Koinuma, J. Appl. Phys. 87, 1844 (2000).
[4] F. Spaziani, M. C. Rossi, S. Salvatori, G. Conte, and P. Ascarelli, Appl. Phys. Lett. 82, 3785 (2003).
[5] W. Yang, R. D. Vispute, S. Choopun, R. P. Sharma, T. Venkatesan, and H. Shen, Appl. Phys. Lett. 78, 2787 (2001).
[6] M. Mikulics, M. Marso, P. Javorka, P. Kordoš, H. Lüth, M. Koèan, A. Rizzi, S. Wu, and R. Sobolewski, Appl. Phys. Lett. 86, 211110 (2005).
[7] W. R. Donaldson, A. M. Kadin, P. H. Ballentine and R. Sobolewski, Appl. Phys. Lett. 54 2470 (1989).
[8] M. Johnson, Appl. Phys. Lett. 59, 1371 (1991).
[9] F. A. Hegmann, R. A. Hughes and J. S. Preston, Appl. Phys. Lett. 64, 3172 (1994). Hegmann, D. Jacobs-Pekins, C. C. Wang, S. H. Moffat, R. A. Hughes, J. S. Preston, M. Currie, P. M. Fauchet, T. Y. Hsiang and R. Sobolewski, Appl. Phys. Lett. 67, 285 (1995).
[10] M. Lindgren, V. Trifonov, M. Zorin, M. Danerud, D. Winkler, B. S. Karasik, G. N. Gol'tsman and E. M. Gershenzon, Appl. Phys. Lett. 64, 3036 (1994).
[11] K. Zhao, K. J. Jin, Y. H. Huang, S. Q. Zhao, H. B. Lu, M. He, Z. H. Chen, Y. L. Zhou and G. Z. Yang, Appl. Phys. Lett. 89, 173507 (2006).
[12] K. Zhao, H. B. Lu and M. He, Eur. Phys. J. Appl. Phys. 41, 139–142 (2008).
[13] Z. J. Yue, K. Zhao, S. Q. Zhao, Z. Q. Lu, X. M. Li, H. Ni and A. J. Wang , Journal of Physics D: Appl. Phys. 43, 015104 (2010).
[14] H. Liu, K. Zhao, S. Q. Zhao, N. Zhou, H. Zhao, Z. Q. Lu and A. J. Wang, Journal of Physics D: Appl. Phys. 42, 075104 (2009).
[15] X. M. Li, K. Zhao, H. Ni, S. Q. Zhao, W. F. Xiang, Z. Q. Lu, Z. J. Yue, F. Wang, Y. C. Kong and H. K. Wong, Appl. Phys. Lett. 97, 044104 (2010).
[16] Z. J. Yue, K. Zhao, H. Ni, S. Q. Zhao, Y. C. Kong, H. K. Wong and A. J. Wang, Journal of Physics D: Appl. Phys. 44, 095103 (2011).
[17] S. H. Nam and H. G. Kim, J. Appl. Phys. 72, 2895 (1992).
[18] G. M. Rao and S. B. Krupanidhi, J. Appl. Phys. 75, 2604 (1994).
[19] M. H. Yeh, K. S. Liu and I. Nan, Jpn. J. Appl. Phys., Part 1 34, 2247 (1995).
[20] F. J. Walker, R. A. Mckee, H. W. Yen and D. E. Zelmon, Appl. Phys. Lett. 65, 1495 (1994).
[21] T. Hasegawa, S. Mouri, Y. Yamada and K. Tanaka, J. Phys. Soc. Jpn. 72, 41 (2003).
[22] H. Lengfellner, G. Kremb, A. Schnellbögl, J. Betz, K. F. Renk, and W. Prettl, Appl. Phys. Lett. 60, 501 (1992).

[23] N. Zhou, K. Zhao, H. Liu, Z. Q. Lu, H. Zhao, L. Tian, W. W. Liu and S. Q. Zhao, J. Appl. Phys. 105, 083110 (2009).
[24] Z. Q. Lu, K. Zhao, H. Zhao, S. Q. Zhao and Q. L. Zhou, Chinese Physics B, 18(10), 4521-4523 (2009).
[25] H. Zhao, K. Zhao, Z. Q. Lu and S. Q. Zhao http://www.paper.edu.cn/en/, (2009).
[26] T. Tomita, H. Utsunomiya, Y. Kamakura and K. Taniguchi, Appl. Phys. Lett. 71, 3664 (1997).
[27] D. Heh, E. M. Vogel and J. B. Bernstein, Appl. Phys. Lett. 82, 3242 (2003).
[28] C. R. Newman, R. J. Chesterfield, J. A. Merlo and C. D. Frisbie, Appl. Phys. Lett. 85, 422 (2004).
[29] W. J. Turner, Phys. Rev. 101, 1653 (1956).
[30] M. Fukuhara and A. Sampei, J. Mater. Sci.—Mater. Electron. 12, 131 (2001).
[31] R. B. Sosman, Trans. Brit. Ceram. Soc. 54, 665 (1955).
[32] T. Gorelik, M. Will, S. Nolte, A. Tuennermann and U. Glatzel Appl. Phys. A 76, 309 (2003).
[33] S. Jin, T. H. Tiefel, M. McCormack, R. A. Fastnacht, R. Ramesh, and L. H. Chen, Science 264, 413 (1994).
[34] H. Tanaka, J. Zhang, and T. Kawai, Phys. Rev. Lett. 88, 27204 (2002).
[35] R. Cauro, A. Gilabert, J. P. Contour, R. Lyonnet, M.-G. Medici, J. C. Grenet, C. Leighton, and I. K. Shuller, Phys. Rev. B 63, 174423 (2001).
[36] H. Katsu, H. Tanaka, and T. Kawai, Appl. Phys. Lett. 76, 3245 (2000).
[37] M. Rajeswari, C. H. Chen, A. Goyal, C. Kwon, M. C. Robson, R. Ramesh, T. Venkatesan, and S. Lakeou, Appl. Phys. Lett. 68, 3555 (1996).
[38] L. Méchin, J.-M. Routoure, B. Guillet, F. Yang, S. Flament, and D. Robbes, Appl. Phys. Lett. 87, 204103 (2005).
[39] X. T. Zeng and H. K. Wong, Appl. Phys. Lett. 66, 3371 (1995).
[40] J. H. Lim, C. K. Kang, K. K. Kim, I. K. Park, D. K. Hwang and S. J. Park, Adv. Mater. 18, 2720 (2006).
[41] Z. Ye, J. G. Lu, Y.Z. Zhang, Y. J. Zeng, L. L. Chen, F. Zhuge, G. D. Yuan, H. P. He, L. P. Zhu, J. Y. Huang and B. H. Zhao, Appl. Phys. Lett. 91, 113503 (2007).
[42] S. Y. Myong, S. J. Baik, C. H. Lee, W. Y. Cho and K. S. Lim, Jpn. J. Appl. Phys. Part 2 36, L1078 (1997).
[43] B. M. Ataev, A. M. Bagamadova, A.M. Djabrailov, V. V. Mamedo and R. A. Rabadanov, Thin Solid Films 260,19 (1995).
[44] W. W. Liu, S. Q. Zhao, K. Zhao, W. Sun, Y. L. Zhou, K. J. Jin, H. B. Lu, M. He and G. Z. Yang, Physica B 404, 1550-1552 (2009).
[45] S. Q. Zhao, Y. L. Zhou, K. Zhao, Z. Liu, P. Han, S. F. Wang, W. F. Xiang, Z. H. Chen, H. B. Lu, B. L. Cheng and G. Z. Yang, Physica B 373, 154 (2006).
[46] S. T. Kuo, W. H. Tuan, J. Shieh and S. F. Wang, J. Eur. Ceram. Soc 27, 4526 (2007).
[47] S. Jin, T. H. Tiefel, M. McCormack, R. A. Fastnacht, R. Ramesh, and L. H. Chen, Science 264, 413 (1994).
[48] A. Moreo, S. Yunoki, and E. Dagotto, Science 283, 2034 (1999).
[49] M. B. Salamon and M. Jaime, Rev. Mod. Phys. 73, 583 (2001).
[50] Q. L. Zhou, K. Zhao, K. J. Jin, D. Y. Guan, H. B. Lu, Z. H. Chen, G. Z. Yang, A. Li and H. K. Wong, Appl. Phys. Lett. 87, 172510 (2005).

[51] P. L. Lang, Y. G. Zhao, C. M. Xiong, P. Wang, J. Li and D. N. Zheng, J. Appl. Phys. 100, 053909 (2006).
[52] J. R. Sun, C. M. Xiong and B. G. Shen, Appl. Phys. Lett. 85, 4977 (2004).
[53] R. W. Li, H. B. Wang, X. W. Wang, X. Z. Yu, Y. Matsui, Z. H. Cheng, B. G. Shen, E. W. Plummer and J. D. Zhang, Proc. Natl Acad. Sci. 106, 14224 (2008).
[54] I. Genish, Y. Kats, L. Klein, J. W. Reiner and M. R. Beasley, J. Appl. Phys. 95 6681 (2004).
[55] C. Prados, D. V. Dimitrov, C. Y. Ni, A. Hernando and G. C. Hadjipanayis, Phys. Rev. B 56 14076 (1997).
[56] F. Lesmes, A. Salcedo, J. J. Freijo, D. Garcia, A. Hernando and C. Prados, Appl. Phys. Lett. 69 2596 (1996).

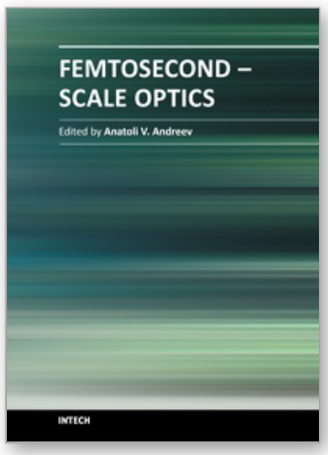

Femtosecond-Scale Optics
Edited by Prof. Anatoly Andreev

ISBN 978-953-307-769-7
Hard cover, 434 pages
Publisher InTech
Published online 14, November, 2011
Published in print edition November, 2011

With progress in ultrashort ultraintense laser technologies the peak power of a laser pulse increases year by year. These new instruments accessible to a large community of researchers revolutionized experiments in nonlinear optics because when laser pulse intensity exceeds or even approaches intra-atomic field strength the new physical picture of light-matter interaction appears. Laser radiation is efficiently transformed into fluxes of charged or neutral particles and the very wide band of electromagnetic emission (from THz up to x-rays) is observed. The traditional phenomena of nonlinear optics as harmonic generation, self-focusing, ionization, etc, demonstrate the drastically different dependency on the laser pulse intensity in contrast the well known rules. This field of researches is in rapid progress now. The presented papers provide a description of recent developments and original results obtained by authors in some specific areas of this very wide scientific field. We hope that the Volume will be of interest for those specialized in the subject of laser-matter interactions.

How to reference
In order to correctly reference this scholarly work, feel free to copy and paste the following:

Hao Ni and Kun Zhao (2011). Ultrafast Photoelectric Effect in Oxide Single Crystals and Films, Femtosecond-Scale Optics, Prof. Anatoly Andreev (Ed.), ISBN: 978-953-307-769-7, InTech, Available from: http://www.intechopen.com/books/femtosecond-scale-optics/ultrafast-photoelectric-effect-in-oxide-single-crystals-and-films

INTECH
open science | open minds

InTech Europe
University Campus STeP Ri
Slavka Krautzeka 83/A
51000 Rijeka, Croatia
Phone: +385 (51) 770 447
Fax: +385 (51) 686 166
www.intechopen.com

InTech China
Unit 405, Office Block, Hotel Equatorial Shanghai
No.65, Yan An Road (West), Shanghai, 200040, China
中国上海市延安西路65号上海国际贵都大饭店办公楼405单元
Phone: +86-21-62489820
Fax: +86-21-62489821

IntechOpen